Data-Driven Aortic Pressure Curve Reconstruction using Electrical Impedance Measurements

Jacob P. Thönes[1], Henryk Richter[1], Patricia Fuchs[1], Lisa Krukewitt[1], Fabian Mueller-Graf[2], Amelie R. Zitzmann[2], Stephan H. Böhm[2], Daniel A. Reuter[2], Volker Kuehn[1], Sascha Spors[1]
[1]*Institute of Communications Engineering, University of Rostock, Germany*
[2]*Department of Anesthesiology, University Medical Center Rostock, Germany*
jacob.thoenes@uni-rostock.de

***Abstract*—Measuring perfusion parameters is crucial for continuous cardiovascular monitoring and early detection of hemodynamic instability. Traditional methods for estimating aortic pressure often rely on invasive procedures, limiting their applicability in real-time, non-invasive monitoring scenarios. This work presents a novel data-driven approach for reconstructing the aortic pressure curve (APC) using electrical impedance tomography (EIT) measurements. Therefore, a reconstruction model based on a variational autoencoder (VAE) and a deep neural network (DNN) is designed and trained. Experimental pig data is used for training, and an extensive hyperparameter search is conducted. The provided results demonstrate that the proposed approach can predict APCs, offering a promising non-invasive alternative for cardiovascular monitoring.**

***Index Terms*—EIT, Data-Driven, Aortic Pressure Estimation**

I. Introduction

Electrical impedance tomography (EIT) is an imaging technique commonly used to determine the spatial impedance distribution within an area of interest [1]. Therefore, surface electrodes are attached to a subject, and low alternating electrical currents are injected through selected electrode combinations. The voltages can be measured between the non-injecting remaining boundary electrodes. Depending on the cross-sectional conductivity distribution, the current flow affects the voltages measured at the surface electrodes [2]. The voltage measurements can be reconstructed to an image of the cross-sectional conductivity distribution by solving the ill-posed, nonlinear inverse EIT problem [2]. The reconstructed images provide valuable insights into the internal structure of the object [1], [2].

EIT has found significant application in medical imaging, particularly in monitoring lung ventilation and diagnosing lung diseases [3], [4]. Here, the electrode belt is attached to the thorax of the human body [5]. Additionally, EIT is non-invasive and radiation-free, and its portability makes it an ideal candidate for bedside applications, especially in Intensive Care Units (ICUs) [6]. The technique has been shown to effectively detect both physiological and pathophysiological changes in regional pulmonary ventilation, making it particularly valuable for monitoring patients with respiratory disease [6]. EIT has already been used for pulmonary perfusion [7], [8], and also cardiac output and stroke volume measurements [9]. It also enables pressure monitoring in the aorta [10], [11], which is crucial for assessing hemodynamic stability and guiding fluid management. Additionally, the course of aortic pressure over a cardiac cycle provides hemodynamic information supporting disease monitoring and targeting. In clinical practice, aortic pressure is mainly measured by invasive catheters or other non-invasive methods like sphygmomanometry, which require calibration and intensive training or show inaccuracies. Therefore, the demand for non-invasive measurement tools remains [12]. The challenges of using EIT, for example, as an imaging technique in the medical field, are related to the ill-posedness and nonlinearity of the inverse problem. Furthermore, mapping EIT signals to the aortic pressure curve (APC) is difficult due to the complex relationship between impedance changes and hemodynamic parameters, as well as the influence of surrounding tissues and motion artifacts on the signal.

The ill-posed nonlinear inverse EIT problem is addressed using a combination of a variational autoencoder (VAE) and a mapper to reconstruct the aortic blood pressure curve. The VAE model leverages the advantage of learning a low-dimensional manifold of approximate solutions, effectively transforming the ill-posed problem into a well-posed one [13]. The mapper predicts the low-dimensional representation for the final reconstruction of the APC. Full model code is available [14].

II. Methods

A. Reconstruction network architecture

The proposed reconstruction network for the prediction of the APC from EIT measurements is shown in Fig. 1.

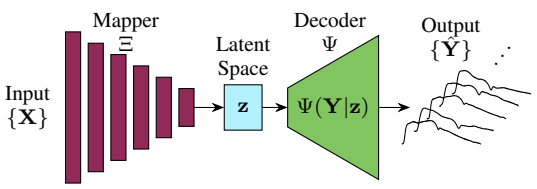

Fig. 1. Network architecture of the proposed network for reconstructing the APC from EIT measurements, consisting of a mapper and the decoder part of a VAE.

It is created based on two consecutive trained networks. First, a VAE is trained unsupervised to learn a low-dimensional

representation of the APC. Second, a mapper is trained supervised using the EIT measurements with the corresponding low-dimensional representation of the APC. The final reconstruction model is created in the third step to predict the APC from the underlying EIT measurements.

1) Variational autoencoder: VAEs have become a prominent method for unsupervised feature extraction, dimensionality reduction, and generative modelling, demonstrating strong efficacy across diverse applications [15]–[17]. In this approach, the VAE is used to learn a low-dimensional representation, also called a latent representation, of the APCs by maximizing the marginal logarithmic likelihood of the provided training data [18]. This process is based on autoencoding, which transforms high-dimensional data into a lower-dimensional representation that can approximate the original observations [18]. The VAE combines Bayesian methods with the flexibility of artificial neural networks, facilitating dimensionality reduction while allowing reconstruction of the data from its low-dimensional latent representation [17].

The VAE model includes two main network components. An encoder Φ, which maps the input data $\mathbf{Y}$ to a latent vector $\mathbf{z}$, and a decoder Ψ, which reconstructs the output $\hat{\mathbf{Y}}$ from $\mathbf{z}$, cf. Fig. 2.

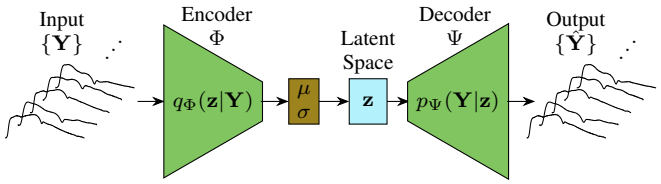

Fig. 2. VAE for learning a latent representation of the APC. Preprocessed pressure curve segments are encoded into a low-dimensional latent space, which the decoder reconstructs by minimizing the error between input and output during training.

An important feature of the used VAE is the inclusion of the β parameter in the loss function

$$(\Phi,\Psi) = \underset{(\Phi,\Psi)\in\mathbb{VAE}}{\operatorname{argmin}} \frac{1}{N}\sum_{n=0}^{N-1}[\| \Psi(\Phi(\mathbf{Y}_n)) - \mathbf{Y}_n \|^2 + \beta\, D_{\mathrm{KL}}(q_\Phi(\mathbf{z}_n|\mathbf{Y}_n) \parallel p_\Psi(\mathbf{z}_n))] \quad (1)$$

that is minimized during training [13]. This parameter shapes the latent space by imposing a prior Gaussian distribution, which controls the distribution of latent representations and thus contributes to a more structured latent space [17], [19]. This is achieved by minimizing the Kullback-Leibler (KL) divergence D_{KL}, a measure of statistical distance between $q_\Phi(\mathbf{z}|\mathbf{Y})$ and $p_\Psi(\mathbf{z})$, thereby optimizing the match between the two distributions [17], [20]. A $\beta > 1$ imposes stronger constraints on the posterior $q_\Phi(\mathbf{z}|\mathbf{Y})$, and the regularization is strengthened, leading to a more structured latent space at the potential cost of reconstruction quality [17], [19]. Conversely, if $\beta < 1$, the regularization is down-weighted, which can improve the reconstruction quality but may result in a less structured latent space. During the implementation and hyperparameter tuning in II-D of the VAE, the challenge is finding a balance between the reconstruction and regularization terms [17].

2) Mapper: The mapper Ξ, composed of convolutional neural network (CNN) layers and a deep neural network (DNN) output layer, is trained supervised to learn a connection between the EIT measurement $\mathbf{X}$ and the latent space $\mathbf{z} = \Phi(\mathbf{Y})$ provided by the VAE encoder part. The mapper has the advantage of learning a compact encoding rather than attempting the direct reconstruction [13]. The exact layer configuration and parameters are determined during the hyperparameter tuning, described in II-D.

B. Instrumentation and recording of animal data

The data utilized for model training were collected in a previous study investigating drug-induced pulmonary hypertension [21], [22]. The experimental protocol involved ten German Landrace pigs, aged 12 to 16 weeks, which were anesthetized and instrumented for the study. For EIT data acquisition, an elastic, custom-made EIT belt equipped with 32 electrodes was placed around the thorax of each animal, centered at the level of the heart. To acquire the pressure data, the pigs were equipped with different catheter types. X-ray was employed to confirm the correct placement of both the catheters and the EIT belt. A high-sensitivity pressure sensor catheter (Mikro-Tip® SPR-350, Millar Instruments Inc., Houston, TX, USA), measuring 5 Charrière (Ch), was placed via the left femoral artery to monitor pressure in the descending aorta. This catheter is hereinafter referred to as the "MEMS catheter". Additionally, a 4 Ch 16 cm PiCCO® catheter (Getinge AB, Gothenburg, Sweden) or an equivalent arterial line was inserted through the right carotid artery to measure pressure in the descending aorta. This catheter is hereinafter referred to as the "fluid catheter".

EIT data were recorded at a rate of 47.68 Hz using the Swisstom EIT Pioneer Set (Swisstom AG, EIT branch, Landquart, Switzerland). Concurrently, catheter-based measurements were collected at a sampling rate of 1 kHz using the ADInstruments PowerLab 16/35 system (ADInstruments, Dunedin, New Zealand). The original study involved up to nine distinct pulmonary arterial pressure states for each animal [21], [22]. Each of these distinct pulmonary arterial pressure states is called a "block". More detailed information about sedation, anesthesia, preparation, and catheterization of the animal model can be found in [21].

The study was approved by the governmental ethical board for animal research (Landesamt für Landwirtschaft, Lebensmittelsicherheit und Fischerei, Mecklenburg-Vorpommern, Germany; No: 7221.3-1-037) and was carried out under the EU-directive 2010/63/EU and the Animal Research: Reporting of In Vivo Experiments guidelines 2.0 (ARRIVE 2.0).

C. Data processing

Data processing aims to create a data set consisting of samples containing EIT measurements aligned with their corresponding APCs. A primary challenge is to segment the EIT

and LabChart measurements into correctly coupled frames. A single frame is defined as a complete APC corresponding to one heartbeat, along with the EIT measurements taken during that time. Samples differ from frames in that they contain preprocessed frame data. The variability of heart rates and the absence of synchronization during data acquisition necessitate preprocessing and quality checks to ensure the accuracy and consistency of the samples.

1) Synchronization: During data recording, an external manual trigger by the Pioneer Set was used to synchronize EIT measurements with ADInstruments PowerLab data, generating synchronization pulses recorded on a dedicated PowerLab channel. Inconsistencies in the initial timestamps required an alignment by identifying synchronization marks in both the EIT and the LabChart data sets. Furthermore, due to the animals' underlying vital conditions, experiments were re-enacted, and not all EIT files were retained, leading to mismatches in synchronization markers. Consequently, some synchronization pulses were absent in the EIT recordings. To address this, individual synchronization was performed for each EIT measurement. The first dimension of the EIT frame is constant. It corresponds to the number of electrodes ($L = 32$) attached to the pigs during the measurement, resulting in a constant dimension of $L^2 = 1024$ for all possible electrode injection combinations. The second dimension of the EIT frame corresponds to the length of the temporal EIT data sequence recorded during a single heartbeat. Temporal drift issues were mitigated using a synchronization protocol that included an initial pulse marking the start of the EIT recording, a final pulse indicating the end, and a sample-by-sample timing recovery process.

2) Catheter calibration: The aortic pressure signals were measured from two arterial catheters: fluid-filled and MEMS-based. The fluid-filled catheter provided stable measurements but was affected by fluid resonance effects [23]. The MEMS catheter delivered artifact-free pressure curves but exhibited drift over time. To address this drift, a recalibration procedure was implemented using the fluid catheter as a reference, assuming a consistent drift within each EIT measurement. The process involved three steps: temporal alignment, filtering, and robust mean estimation. The temporal alignment using cross-correlation corrected for minor placement differences between the catheters, accounting for pulse wave velocity variations [24]. A median filter ($100\,\mathrm{ms}$) was applied to both signals to suppress fluid resonance effects. Following this, a robust mean estimation was conducted to handle potential artifacts caused by the movement of subjects or other interference. A robust M-estimator using Tukey's weight method was used to suppress outliers and iteratively adjust the drift estimate.

3) Segmentation: A segmentation approach in the frequency domain was employed without EIT image reconstruction for heartbeat-by-heartbeat estimation of the APC from EIT data. The method utilized the Fourier-based Synchrosqueezing Transform (SST) [25] to extract individual heartbeat intervals from the mixed EIT signals. This transform represented the input signal as a combination of multiple components and mapped it onto the time-frequency plane, enhancing the detection of dominant frequency components corresponding to heartbeats [25].

The SST method remaps the short-time Fourier transform coefficients to obtain a refined representation of local instantaneous frequencies. This allowed for precise tracking of heart rate changes even under non-stationary conditions. Potential issues, such as misdetection due to abrupt rate changes, were mitigated by applying a low-pass filter to stabilize frequency estimates.

The resulting spectrogram's instantaneous frequency representing the heart rate was iteratively extracted using a local search algorithm. Typically, three to five iterations were sufficient for a stable estimation from the MEMS catheter signal. The phase information was subsequently derived, enabling the identification of individual heartbeats through zero-crossing detection of the estimated phase signal. This approach facilitated accurate temporal segmentation of EIT data, aligning each extracted interval with corresponding heartbeats for further analysis.

4) Segment post processing: Particularly at low APCs, occasional extrasystoles were observed in the data set. Extrasystoles are characterized by a distinct pattern: a lower aortic pressure variation followed by a larger variation in the subsequent cycle. For each measurement channel, the mean and maximum signals were compiled into matrices, and their first derivatives were calculated to detect abrupt changes while minimizing drift influence. Thresholds were established based on deviations from the average signal amplitude to identify outliers. Using these thresholds, extrasystoles and their subsequent beats were flagged as outliers. These identified segments were excluded from the data set to ensure the focus remained on regular heartbeats.

During data processing, segments in the EIT recordings appeared affected by external influences such as poor electrode contacts or measurement noise. A single electrode affects 124 of the 1024 channels, highlighting the impact on the data. To address this issue, an additional quality check was implemented. This check was structured to first roughly presort possible corrupt segments, extend individual segments to consecutive segment sections, and separate corrupt segments from valid ones. The identified faulted EIT segments were removed from the data set along with their corresponding APC segments to ensure the quality of the data pool.

5) Training data preparation: The final preprocessing step was resampling and normalization of the data. The resampling was necessary to adapt the data shape to the shape of the input and output layers of the utilized reconstruction networks. The EIT data was resampled along the time dimension. This dimension has an inconsistent length due to the previously applied segmentation. All EIT frames were resampled to a constant shape of $\mathbf{x} \in \mathbb{R}^{64\times1024}$. The temporal EIT dimension value of 64 was chosen as the closest power of two that exceeded the maximum length value of the data set along this axis, which was 41. The APC frames were resampled to a constant length of $\mathbf{y} \in \mathbb{R}^{1024\times1}$, chosen as the closest power

of two that exceeded the maximum length value of the aortic pressure segments, which was precisely 1024.

Furthermore, a block-wise z-score normalization of the EIT data was conducted. APC segments were normalized by subtracting 85 and dividing by 20 for each sample. These values were chosen heuristically by manually evaluating a histogram of the amplitude distribution of all APC segments. This normalization can be easily inverted for later evaluation of the test data to obtain the original range of values. The preprocessed EIT data is described by $\mathbf{X} = \{\mathbf{x}_1, \mathbf{x}_2, \cdots, \mathbf{x}_N\}$ and the preprocessed APC is described by $\mathbf{Y} = \{\mathbf{y}_1, \mathbf{y}_2, \cdots, \mathbf{y}_N\}$. The final data set consists of the whole preprocessed data samples of ten pigs and is described by $\{\mathbf{X}, \mathbf{Y}\}_{n=1}^{N}$.

D. Training and hyperparameter tuning

All data samples from pig one to pig nine are used for training and validation, which results in $N = 73\,536$ samples. The training set consists of $80\,\%$ randomly selected samples, and the validation set consists of the remaining $20\,\%$ of this data subset. Pig ten is used as test data to evaluate the robustness of the network architecture on an unknown individual. If the trained model generalizes well, it will be able to predict APCs from EIT measurements even for unknown individual pigs, such as pig ten.

First, the VAE is trained on the prepared aortic segments $\{\mathbf{Y}\}$. In the second step, the mapper is trained with the EIT data and the corresponding latent representation, created by the VAE $\mathbf{z} = \Phi(\mathbf{Y})$, which results in a supervised training set $\{\mathbf{X}, \mathbf{z}\}$. Both networks are created with *Tensorflow* and tuned with the grid search in *Kerastuner*. During this tuning process, the number of layers, kernel size, filter size, strides, padding, dropout, activation, and other network parameters are evaluated systematically. The VAE and the mapper networks are re-initialized and trained based on the best parameters obtained from the hyperparameter tuning. The final network architectures of the VAE and the mapper are documented in [14].

III. Results

Fig. 3 visualizes a temporal sequence of nine reconstructed APCs from unknown EIT measurements of pig ten. It can be seen that the shape of the APC can be reconstructed successfully by the trained model. It should also be mentioned that any temporal correlations were excluded by random shuffling of the training data. Furthermore, the model created is also sensitive to the reconstruction of the pig's respiratory function, as can be seen from the increasing tendency of the amplitude of the predicted heartbeat segments compared to the known heartbeat segments. From Fig. 3, it can be seen that the model has successfully generalized and can predict the APCs from the EIT measurements of the unknown individual pig.

Some statistics are computed for the full test data set to obtain a more general performance evaluation. Fig. 4 illustrates the absolute value of the relative error profiles for two

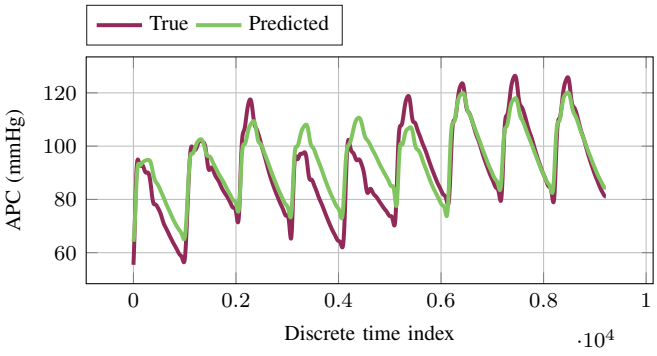

Fig. 3. Predictions of the APC by the final trained reconstruction model with the corresponding actual APC for nine consecutive EIT measurements of the test pig.

statistical measures. Therefore the error matrix $\mathbf{E}$ is computed element-wise as

$$\mathbf{E} = \left| \frac{\mathbf{Y}_{\text{pred}} - \mathbf{Y}_{\text{true}}}{\mathbf{Y}_{\text{true}}} \right| \tag{2}$$

where $\mathbf{Y}_{\text{true}}$ and $\mathbf{Y}_{\text{pred}}$ are matrices structured such that their rows contain the APCs, while the number of rows represents the number of test data of the true and predicted APCs. Furthermore, the mean error $\mu_{\mathbf{E}}$, and the standard deviation $\sigma^2_{\mathbf{E}}$ along the resampled aorta pressure curve index k of each aorta segment are computed.

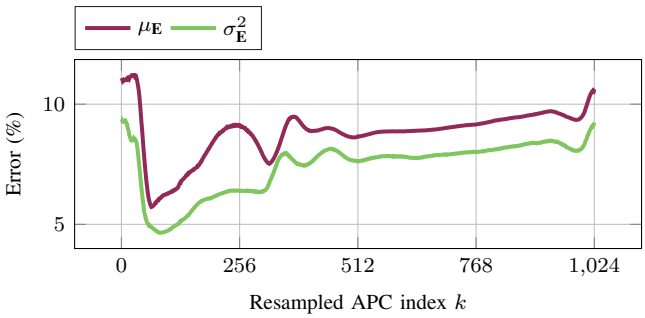

Fig. 4. Error visualization of mean $\mu_{\mathbf{E}}$ and standard deviation $\sigma^2_{\mathbf{E}}$ of the error matrix $\mathbf{E}$ along the resampled aorta pressure curve index k.

The trend of the mean error curve indicates a systematic offset in the reconstruction process. The standard deviation of the error $\sigma^2_{\mathbf{E}}$ is relatively high at the beginning, indicating higher variability in the reconstruction errors in the initial indices. This behavior suggests local inaccuracies that persist consistently throughout the curve. The higher error values at the beginning and end of a segment show that the boundaries of the individual aortic curves are still a challenge for the model. The systematic bias in the mean $\mu_{\mathbf{E}}$ and the standard deviation $\sigma^2_{\mathbf{E}}$ suggests areas for improvement, particularly in minimizing inaccuracies and correcting the bias trend.

It should be mentioned that the data set used for training exhibits imbalance in two key aspects: the number of samples per pig is inconsistent, and the distribution of samples is

uneven across low and high APCs and very low and high respiratory rates. As a result, the VAE does not learn all curve properties with the exact weighting. One way of compensating for the different numbers of samples per pig would be to expand the data set using data augmentation techniques. In addition, the inaccuracies of the VAE have to be mentioned as an error propagation for the mapper's training.

IV. Conclusion

Although more research is needed, the results can be interpreted as positive with potential. This approach can potentially improve patient safety and the responsiveness of clinical interventions by providing continuous and reliable APC estimates using EIT. Above all, the available data is key for expanding and further testing this approach. To improve the robustness of the models, more data from more individuals should be used for training, and imbalances should be compensated.

Another challenge of this approach lies in the proper amplitude scaling of the pressure curve and the right, well-chosen normalization process. For future work, a challenge remains in processing APCs and EIT measurements without needing time-dimension resampling. Overcoming these challenges is essential to advance the integration of these technologies into robust, real-time monitoring systems for clinical and ambulatory settings. Consistent with other results in the literature, EIT also provides, in this case, the potential for concurrent detection of regional changes due to ventilation and perfusion, which could enhance the evaluation of lung function in clinical settings [6]. To improve the accuracy of this reconstruction approach in the future, a time series of EIT measurements could be fed into the model to improve the prediction accuracy using recurrent neural networks, such as long short-term memories.

Acknowledgment

Funded by the Deutsche Forschungsgemeinschaft (DFG, German Research Foundation) – SFB 1270/2 - 299150580.

References

[1] A. Adler and D. Holder, *Electrical impedance tomography: methods, history and applications*. CRC Press, 2021.

[2] B. Eyuboglu, B. Brown, and D. Barber, "In vivo imaging of cardiac related impedance changes," *IEEE Engineering in Medicine and Biology Magazine*, vol. 8, no. 1, pp. 39–45, 1989.

[3] T. K. Bera, "Applications of electrical impedance tomography (eit): a short review," in *IOP Conference Series: Materials Science and Engineering*, vol. 331, p. 012004, IOP Publishing, 2018.

[4] H. Yu, H. Liu, Z. Liu, Z. Wang, and J. Jia, "High-resolution conductivity reconstruction by electrical impedance tomography using structure-aware hybrid-fusion learning," *Computer Methods and Programs in Biomedicine*, vol. 243, p. 107861, 2024.

[5] G. Saulnier, R. Blue, J. Newell, D. Isaacson, and P. Edic, "Electrical impedance tomography," *IEEE Signal Processing Magazine*, vol. 18, no. 6, pp. 31–43, 2001.

[6] D. Nguyen, C. Jin, A. Thiagalingam, and A. McEwan, "A review on electrical impedance tomography for pulmonary perfusion imaging," *Physiological measurement*, vol. 33, no. 5, p. 695, 2012.

[7] A. Fagerberg, O. Stenqvist, and A. Aneman, "Monitoring pulmonary perfusion by electrical impedance tomography: an evaluation in a pig model," *Acta Anaesthesiologica Scandinavica*, vol. 53, no. 2, pp. 152–158, 2009.

[8] J. B. Borges, F. Suarez-Sipmann, S. H. Bohm, G. Tusman, A. Melo, E. Maripuu, M. Sandström, M. Park, E. L. V. Costa, G. Hedenstierna, and M. Amato, "Regional lung perfusion estimated by electrical impedance tomography in a piglet model of lung collapse," *Journal of applied physiology (Bethesda, Md. : 1985)*, vol. 112, no. 1, pp. 225–236, 2012.

[9] R. Pikkemaat, S. Lundin, O. Stenqvist, R.-D. Hilgers, and S. Leonhardt, "Recent advances in and limitations of cardiac output monitoring by means of electrical impedance tomography," *Anesthesia and analgesia*, vol. 119, no. 1, pp. 76–83, 2014.

[10] J. Solà, A. Adler, A. Santos, G. Tusman, F. S. Sipmann, and S. H. Bohm, "Non-invasive monitoring of central blood pressure by electrical impedance tomography: first experimental evidence," *Medical & Biological Engineering & Computing*, vol. 49, p. 409, Mar 2011.

[11] F. Braun, M. Proença, M. Rapin, M. Lemay, A. Adler, B. Grychtol, J. Solà, and J.-P. Thiran, "Aortic blood pressure measured via EIT: investigation of different measurement settings," *Physiological Measurement*, vol. 36, pp. 1147–1159, may 2015.

[12] E. Agabiti-Rosei, G. Mancia, M. F. O'Rourke, M. J. Roman, M. E. Safar, H. Smulyan, J.-G. Wang, I. B. Wilkinson, B. Williams, and C. Vlachopoulos, "Central blood pressure measurements and antihypertensive therapy: a consensus document," *Hypertension*, vol. 50, no. 1, pp. 154–160, 2007.

[13] J. K. Seo, K. C. Kim, A. Jargal, K. Lee, and B. Harrach, "A learning-based method for solving ill-posed nonlinear inverse problems: A simulation study of lung eit," *SIAM journal on Imaging Sciences*, vol. 12, no. 3, pp. 1275–1295, 2019.

[14] J. Thönes, "Data-Driven-Aortic-Pressure-Curve-Reconstruction-using-Electrical-Impedance-Measurements." https://github.com/EITLabworks/Data-Driven-Aortic-Pressure-Curve-Reconstruction-using-Electrical-Impedance-Measurements, 2025.

[15] J. Thönes and S. Spors, "Data-driven 3d reconstruction for electrical impedance tomography," in *2024 46th Annual International Conference of the IEEE Engineering in Medicine and Biology Society (EMBC)*, pp. 1–4, 2024.

[16] D. P. Kingma, "Auto-encoding variational bayes," *arXiv preprint arXiv:1312.6114*, 2013.

[17] R. Zemouri, M. Lévesque, É. Boucher, M. Kirouac, F. Lafleur, S. Bernier, and A. Merkhouf, "Recent research and applications in variational autoencoders for industrial prognosis and health management: A survey," in *2022 Prognostics and Health Management Conference (PHM-2022 London)*, pp. 193–203, 2022.

[18] M. Tschannen, O. Bachem, and M. Lucic, "Recent advances in autoencoder-based representation learning," *arXiv preprint arXiv:1812.05069*, 2018.

[19] C. P. Burgess, I. Higgins, A. Pal, L. Matthey, N. Watters, G. Desjardins, and A. Lerchner, "Understanding disentangling in β-VAE," *preprint arXiv:1804.03599*, 2018.

[20] C. Doersch, "Tutorial on variational autoencoders," *arXiv preprint arXiv:1606.05908*, 2016.

[21] F. Mueller-Graf, J. Merz, T. Bandorf, C. F. Albus, M. Henkel, L. Krukewitt, V. Kuehn, S. Reuter, B. Vollmar, S. Pulletz, *et al.*, "Correlation of pulse wave transit time with pulmonary artery pressure in a porcine model of pulmonary hypertension," *Biomedicines*, vol. 9, no. 9, p. 1212, 2021.

[22] F. Mueller-Graf, P. Frenkel, C. F. Albus, M. Henkel, S. Reuter, B. Vollmar, G. Tusman, A. Adler, S. Pulletz, S. H. Böhm, *et al.*, "Ventilation induces changes in pulse wave transit time in the pulmonary artery," *Biomedicines*, vol. 11, no. 1, p. 182, 2023.

[23] S. Romagnoli, Z. Ricci, D. Quattrone, L. Tofani, O. Tujjar, G. Villa, S. M. Romano, and A. R. De Gaudio, "Accuracy of invasive arterial pressure monitoring in cardiovascular patients: an observational study," *Cricital Care*, vol. 18, no. 644, pp. –, 2014.

[24] R. Shahzad, A. Shankar, R. Amier, R. Nijveldt, J. J. M. Westenberg, A. de Roos, B. P. F. Lelieveldt, and R. J. van der Geest, "Quantification of aortic pulse wave velocity from a population based cohort: a fully automatic method," *Journal of Cardiovascular Magnetic Resonance*, vol. 21, no. 27, pp. –, 2019.

[25] T. Oberlin, S. Meignen, and V. Perrier, "The fourier-based synchrosqueezing transform," in *2014 IEEE International Conference on Acoustics, Speech and Signal Processing (ICASSP)*, pp. 315–319, 2014.